

Article

## Performance Analysis of an Evaporator for a Diesel Engine–Organic Rankine Cycle (ORC) Combined System and Influence of Pressure Drop on the Diesel Engine Operating Characteristics

Chen Bei <sup>1,2</sup>, Hongguang Zhang <sup>1,2,\*</sup>, Fubin Yang <sup>1,2</sup>, Songsong Song <sup>1,2</sup>, Enhua Wang <sup>3</sup>, Hao Liu <sup>1,2</sup>, Ying Chang <sup>1,2</sup>, Hongjin Wang <sup>1,2</sup> and Kai Yang <sup>1,2</sup>

<sup>1</sup> College of Environmental and Energy Engineering, Beijing University of Technology, Pingleyuan No. 100, Beijing 100124, China; E-Mails: bc887410@126.com (C.B.); yangfubinnuc@163.com (F.Y.); qihsong@126.com (S.S.); liuhao\_0225@163.com (H.L.); changying16688@126.com (Y.C.); bjgywanghongjin@163.com (H.W.); ykai104@163.com (K.Y.)

<sup>2</sup> Collaborative Innovation Center of Electric Vehicles in Beijing, Pingleyuan, No. 100, Beijing 100124, China

<sup>3</sup> State Key Laboratory of Automotive Safety and Energy, Tsinghua University, Qinghuayuan, Beijing 100084, China; E-Mail: wangenhua@tsinghua.edu.cn

\* Author to whom correspondence should be addressed; E-Mail: zhanghongguang@bjut.edu.cn; Tel.: +86-10-6739-2469; Fax: +86-10-6739-2774.

Academic Editor: K. T. Chau

Received: 1 May 2015 / Accepted: 1 June 2015 / Published: 8 June 2015

---

**Abstract:** The main purpose of this research is to analyze the performance of an evaporator for the organic Rankine cycle (ORC) system and discuss the influence of the evaporator on the operating characteristics of diesel engine. A simulation model of fin-and-tube evaporator of the ORC system is established by using Fluent software. Then, the flow and heat transfer characteristics of the exhaust at the evaporator shell side are obtained, and then the performance of the fin-and-tube evaporator of the ORC system is analyzed based on the field synergy principle. The field synergy angle ( $\beta$ ) is the intersection angle between the velocity vector and the temperature gradient. When the absolute values of velocity and temperature gradient are constant and  $\beta < 90^\circ$ , heat transfer enhancement can be achieved with the decrease of the  $\beta$ . When the absolute values of velocity and temperature gradient are constant and  $\beta > 90^\circ$ , heat transfer enhancement can be achieved with the increase of the  $\beta$ . Subsequently, the influence of the evaporator of the ORC system on diesel engine

performance is studied. A simulation model of the diesel engine is built by using GT–Power software under various operating conditions, and the variation tendency of engine power, torque, and brake specific fuel consumption (BSFC) are obtained. The variation tendency of the power output and BSFC of diesel engine–ORC combined system are obtained when the evaporation pressure ranges from 1.0 MPa to 3.5 MPa. Results show that the field synergy effect for the areas among the tube bundles of the evaporator main body and the field synergy effect for the areas among the fins on the windward side are satisfactory. However, the field synergy effect in the areas among the fins on the leeward side is weak. As a result of the pressure drop caused by the evaporator of the ORC system, the diesel engine power and torque decreases slightly, whereas the BSFC increases slightly with the increase of exhaust back pressure. With the increase of engine speed, power loss, torque loss, and BSFC increment increase gradually, where the most significant change is less than 1%. Compared with the diesel engine itself, the maximum increase of power output of the diesel engine–ORC combined system is 6.5% and the maximum decrease of BSFC is 6.1%.

**Keywords:** organic Rankine cycle; diesel engine; evaporator; simulation; field synergy; exhaust back pressure

---

## 1. Introduction

Car ownership increases rapidly with economic development. The growing number of cars in use will raise energy consumption and cause serious environmental pollution. Of an engine's fuel combustion energy, only about 30% to 45% is converted into mechanical energy for a diesel engine and about 20% to 30% is converted into mechanical energy for a gasoline engine. About one-third is dissipated in the form of waste heat through the exhaust [1,2]. Therefore, the transformation and utilization of the waste heat of engine exhaust gas is an effective way to improve the efficiency of the engine and reduce fuel consumption and pollutant emissions. Organic Rankine cycle (ORC) is an effective waste heat recovery method that has been widely applied in many domains, such as steel industry [3], cement industry [4], solar-powered plant [5], biomass cogeneration plant [6], internal combustion engine and so on. Uusitalo *et al.* [7] studied the potential for electricity production from the waste heat of large reciprocating engines with the ORC process technology, which is beneficial for increasing the efficiency of the engine power plant. The results showed that the power output of the selected engine can be increased by 11.4% by utilizing exhaust gas heat and 2.4% by utilizing the charge air heat. Leslie *et al.* [8] studied a project demonstrating the technical and economic feasibility of recovering thermal energy from a 27 MW gas turbine driving a natural gas pipeline compressor with an organic Rankine cycle system. The results showed that the organic Rankine cycle system produced 5.5 MW of electricity with no additional fuel consumption and near-zero emissions. The organic Rankine cycle improved the overall energy efficiency by 28%.

A key component of the ORC system, the evaporator has an important influence on the thermal power conversion performance of the ORC system and operating performance of the engine. Imran *et al.* [9] optimized the geometrical parameters of chevron type plate evaporator for a low temperature geothermal ORC system using Non-dominated Sorting Genetic Algorithm-II (NSGA-II). The optimization targets

were pressure drop and cost of evaporator. The results showed that the minimum evaporator cost was \$1570; the pressure drop was 125 kPa. Zhang *et al.* [10] investigated the performance of a finned-tube evaporator used to recover diesel engine exhaust waste heat. The heat transfer area of a fin-and-tube evaporator should be chosen according to the typical operating region of the engine. Kundu *et al.* [11] analyzed the performance and optimum dimensions of flat fins for tube-and-fin heat exchangers through a semi-analytical technique. The optimum dimensions for flat fins of tubes were obtained specifying the ratio of longitudinal to transverse tube pitch. These studies optimize heat exchanger performance through theoretical calculations. However, the flow and heat transfer fields are not discussed.

Several researchers used methods of computational fluid dynamics (CFD) to analyze the flow and heat transfer characteristics of the fluid in the evaporator by establishing a three-dimensional model. Furthermore, guidance for the design of the evaporator was provided. Zhang *et al.* [12] studied experimentally and numerically the heat transfer characteristics of a helically baffled heat exchanger combined with one three-dimensional finned tube. The results showed that the numerical investigations agreed well with the measurements. Ozden *et al.* [13] investigated the shell side design of a shell-and-tube heat exchanger by numerically modeling a small heat exchanger. The flow and temperature fields inside the shell were resolved using a commercial CFD package. The effect of the baffle spacing to shell diameter ratio on the heat exchanger performance was investigated. The results showed that CFD simulations could pinpoint the source and the location of the weakness. The use of CFD together with supporting experiments might speed up the shell-and-tube heat exchanger design process. Zhang *et al.* [14] investigated the performance of several shell-and-tube heat exchangers, one with segmental baffles and four with helical baffles at helix angles of 20°, 30°, 40° and 50°. The results showed that, the heat exchanger with helical baffles of 40° angle showed the best performance among the five heat exchangers that were tested.

Several scholars analyzed the flow and heat transfer characteristics of the tube and fin evaporator through CFD methods. An *et al.* [15] analyzed the detailed phenomenon in a fin-tube heat exchanger, predicted the heat transfer characteristics of the wave-fin heat exchangers using Fluent, and captured the flow characteristics. Bhuiyan *et al.* [16] investigated the heat transfer and fluid flow characteristics of a four-row plain fin-and-tube heat exchanger using the CFD simulations. The effects of Reynolds number, fin pitch, and tube pitches on the overall heat transfer and friction factor for plate fin-and-tube heat exchangers were analyzed.

To optimize the structure of the fin and tube evaporator, several scholars analyzed the effect of the geometry of the fin and tube evaporator on heat transfer performance [17–21]. Tang *et al.* [17] investigated the air-side performance of the fin-and-tube heat exchangers with five types of fin configurations through experimental and numerical methods. The results showed the crimped spiral fin had higher heat transfer and pressure drop than the other four fins. Aytunc *et al.* [18] investigated the influence of the geometric structure of the fin on heat transfer and pressure drop of heat exchanger based on the numerical simulation method using the CFD software. The results indicated that the distance between the fins had a considerable effect on pressure drop and heat transfer by placing the fin-tube in the downstream region positively. Şahin *et al.* [19] investigated the heat transfer and pressure drop of seven different fin angles (0°, 5°, 10°, 15°, 20°, 25°, 30°) with plain fin-tube heat exchangers using Fluent. The results showed that, the heat exchanger with the inclined fin angle of 30° exhibited the maximum heat transfer enhancement.

Several scholars studied the performance of the evaporator for an engine exhaust heat recovery system. Hatami *et al.* [22] separately recycled the exhaust gas energy of gasoline engine and diesel engine by two different evaporators. The evaporators were simulated under three different turbulence models by Fluent software. Then, the variations of the outlet temperatures of the exhaust and the working fluid as functions of the engine torque were obtained. The results showed that the simulation results that selected the SST  $k-\omega$  and RNG  $k-\epsilon$  model were closer to the experimental results. Bai *et al.* [23] designed six different heat exchangers to recover engine exhaust and compare heat transfer and pressure drop by their CFD models. The results showed that the serial plate structure enhanced heat transfer with seven baffles. The maximum heat was 1737 W, and the maximum pressure drop was 9.7 kPa. However, no study reported flow resistance of the evaporator shell side effect on the engine operation performance.

The evaporator of an ORC system is used for engine exhaust heat recovery, which will cause flow resistance of exhaust gas on the evaporator shell side, thereby resulting in increased exhaust back pressure. As a result, engine performance will be affected.

Presently, quite a few scholars have studied evaporator performance from the point of view of engine waste heat recovery. Furthermore, few scholars study the influence of an evaporator on the engine operating performance comprehensively. Therefore, as a heat exchanging component of the ORC system, the evaporator has key effect on the ORC system performance and the diesel engine performance. The main purpose of this research is to analyze the flow and heat transfer characteristics of the exhaust at the evaporator shell side and the influences of an evaporator used for the ORC system on engine performance under various operating conditions.

First, the evaporator simulation model is established by using Fluent software. The specific boundary conditions are based on the data for the selected engine operating point. The temperature field distribution, the pressure field distribution, and the streamlines of the exhaust gas at the evaporator shell side are obtained through evaporator simulation. The heat transfer performance of the evaporator is analyzed by using the field synergy principle. The test bench of the ORC system for the exhaust heat recovery is built to measure the evaporator performance. The Fluent based simulation results are validated by the experimental data. Furthermore, a simulation model of the diesel engine is built by using GT–Power. The GT–Power based simulation results are validated by the experimental data. The influence of the evaporator for ORC system on engine power, torque, and brake specific fuel consumption (BSFC) is studied under various operating conditions. Finally, the variation tendency of the power output and BSFC of the diesel engine–ORC combined system is obtained.

## 2. Numerical Simulation and Performance Analysis of Evaporator

### 2.1. Physical Model of Evaporator

In this research, the flow and heat transfer characteristics of the exhaust at the evaporator shell side are studied by using Fluent software. The half-section physical model of the fin-and-tube evaporator is shown in Figure 1. The evaporator consists of the front end portion, the main body, and the back end portion. The main body is the heat convection place of the exhaust gas and the organic working fluid. The exhaust gas of diesel (hot fluid) is at the evaporator shell side, whereas the organic working fluid (cold fluid) is on the tube side. Both the front and the back end portions are conical pipes, which are

used to connect the main body of the evaporator and the exhaust pipes of the diesel engine. The geometric dimensions of the fin-and-tube evaporator are shown in Table 1.

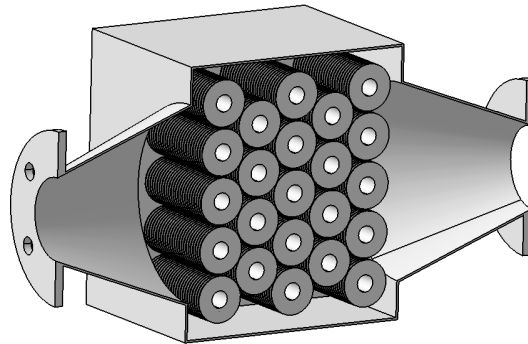


**Figure 1.** Physical model of the fin-and-tube evaporator.

**Table 1.** Geometric dimensions of the fin-and-tube evaporator.

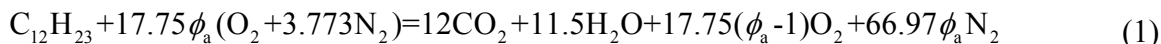
Item	Parameter	Unit
Number of tube rows	5	-
Number of tubes in a row	4 or 5	-
Total number of tubes	23	-
Fin thickness	1.5	mm
Fin height	27	mm
Tube outside diameter	27	mm
Tube inner diameter	20	mm
Tube pitch	$47 \times 56$	mm
Tube row alignment	Staggered	-

A quarter of the physical model of the evaporator for the calculations is used to simplify the numerical calculations and ensure the accuracy of the flow and heat transfer calculation. The assumptions are as follows:

(1) The thermal physical properties of the exhaust gas are set as constants based on the average exhaust temperature; (2) The temperatures of fins, round tubes, and shell are set as constants; (3) The flow of exhaust gas at the evaporator shell side is turbulent, and the flow and heat transfer process is steady; (4) The effect of radiative heat transfer, free convection heat transfer, and gravity on the flow of the engine exhaust gas is ignored.

## 2.2. Boundary Conditions and Governing Equations of the Model

The fin-and-tube evaporator is used to recover the exhaust heat from the diesel engine. The flow and heat transfer characteristics of the engine exhaust at the evaporator shell side at one steady operating point with the engine speed of  $2600 \text{ r} \cdot \text{min}^{-1}$  and the engine torque of  $180.7 \text{ N} \cdot \text{m}$  are studied. The mass flow rate of the intake air and the fuel injection rate are obtained according to the engine test data. The average chemical formula for common fossil diesel fuel can be denoted by  $\text{C}_{12}\text{H}_{23}$  [24]. Based on the atomicity balance principle, the combustion process of diesel fuel with air in the cylinder can be expressed simply as follows:



$\phi_a$  (excess air coefficient) is 1.39. Consequently, the mass fractions for components CO<sub>2</sub>, H<sub>2</sub>O, N<sub>2</sub>, and O<sub>2</sub> can be obtained.

Typically, the exhaust gas temperature is high, and the exhaust gas pressure is slightly higher than the atmospheric pressure (at the inlet of the evaporator). Therefore, exhaust gas can be assumed as a mixture of ideal gases. In this study, the thermal physical properties were calculated based on the average temperature of the exhaust gas at the evaporator shell side. The temperature and pressure of engine exhaust gas can be known by experiment. The density and the specific heat at constant pressure, the thermal conductivity, and the dynamic viscosity for CO<sub>2</sub>, H<sub>2</sub>O, N<sub>2</sub>, and O<sub>2</sub> can be computed by using REFPROP software [25].

The average specific heat at constant pressure of the exhaust gas can be calculated as follows:

$$c_{p,m} = \sum_{i=1}^4 mf_i c_{p,i} \quad (2)$$

The average density of the exhaust gas can be calculated as follows [26]:

$$\rho_m = \frac{\sum_{i=1}^4 mf_i M_i}{\sum_{i=1}^4 mf_i M_i / \rho_i} \quad (3)$$

The average dynamic viscosity of the exhaust gas can be calculated as follows [27]:

$$\mu_m = \frac{\sum_{i=1}^4 \nu f_i \mu_i}{\sum_{j=1}^4 \nu f_j \phi_{ij}} \quad (4)$$

The average thermal conductivity of the exhaust gas can be calculated as follows [27]:

$$\lambda_m = \frac{\sum_{i=1}^4 \nu f_i \lambda_i}{\sum_{j=1}^4 \nu f_j \phi_{ij}} \quad (5)$$

where  $\phi_{ij}$  can be calculated using the following equation:

$$\phi_{ij} = \left( \frac{M_j}{M_i} \right)^{1/2} = \phi_{ji}^{-1} \quad (6)$$

Finally, the thermodynamic properties of the exhaust gas can be obtained, which are listed in Table 2.

**Table 2** Thermodynamic properties of the engine exhaust gas.

Item	Parameter	Unit
Exhaust gas density $\rho_m$	0.6553	kg·m <sup>-3</sup>
Exhaust specific heat at constant pressure $c_{p,m}$	1096.4	J·(kg·K) <sup>-1</sup>
Exhaust thermal conductivity $\lambda_m$	0.04245	W·(m·K) <sup>-1</sup>
Exhaust dynamic viscosity $\mu_m$	$2.8177 \times 10^{-5}$	kg·(m·s) <sup>-1</sup>

The boundary of the inlet of the computational domain is set to the “mass flow inlet” (The “mass flow inlet” is a kind of boundary condition which can be used in FLUENT to provide a prescribed mass flow rate or mass flux distribution at the inlet.) in Fluent software. According to the engine test data, the mass flow rate of the intake air is  $0.06464 \text{ kg}\cdot\text{s}^{-1}$ , the fuel injection rate is  $0.00324 \text{ kg}\cdot\text{s}^{-1}$ , and the exhaust temperature at the inlet of the evaporator is 628 K. The mass flow rate of the exhaust is the summation of the intake air rate and the injected fuel rate, which is  $0.06788 \text{ kg}\cdot\text{s}^{-1}$ . The boundary of the outlet of the computational domain is set to the “pressure outlet” (The “pressure outlet” is a kind of boundary condition which can be used in FLUENT to provide a specification of a static pressure at the outlet.) in Fluent software. The exhaust pressure at the outlet of evaporator is set to the ambient pressure (atmospheric pressure). The abovementioned boundary conditions are summarized in Table 3.

**Table 3** Boundary conditions of the computational domain.

Item	Parameter	Unit
Mass flow rate of exhaust gas	0.06788	$\text{kg}\cdot\text{s}^{-1}$
Temperature at evaporator inlet	628	K
Pressure at evaporator outlet	$1.01 \times 10^5$	Pa

The numerical simulation results based on the standard k- $\epsilon$ , the realizable k- $\epsilon$ , and the RNG k- $\epsilon$  models are compared and discussed. The average exhaust temperature at the evaporator outlet for the standard k- $\epsilon$  model is 488 K, the average exhaust temperature at the evaporator outlet for the RNG k- $\epsilon$  model is 488.4 K, and the average exhaust temperature at the evaporator outlet for the realizable k- $\epsilon$  model is 490.5 K. Among the three models, the average exhaust temperature at the evaporator outlet for the realizable k- $\epsilon$  model is closer to the experimental value. Therefore, the realizable k- $\epsilon$  model is employed during the numerical simulation process. Normally, the standard wall functions in Fluent are used for industrial flows.

### 2.3. Grid Generation and Numerical Method

The geometry model of the fin-and-tube evaporator is established by using CATIA software. To reduce the workload of calculation, we use a quarter of the evaporator’s physical model for calculations based on the principle of symmetry. A 3D grid system is built by using the commercial tool ICEM 14.5. With the use of “Robust (Octree)” mesh method and “tetra/mixed” mesh type, the geometry model is discretized with unstructured elements. The grid of the geometry model for the fin-and-tube evaporator is shown in Figure 2.

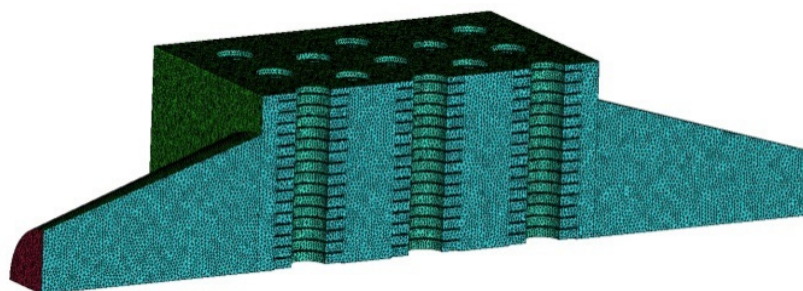


**Figure 2.** Grid of geometry model for the fin-and-tube evaporator.

To ensure the validity and accuracy of the numerical simulation results, the grid-independence of the numerical solutions should be carefully checked [28]. Three different grid systems are employed. The first grid system has 3,128,845 cells. The second grid system has 4,015,918 cells. Finally, the third grid system has 5,338,761 cells. Through the numerical calculation, the exhaust temperatures at the outlet of the evaporator for the three different grid systems can be obtained. The relative error of the average exhaust temperature at the evaporator outlet between the first grid system and the second grid system is 0.20%. The relative error of the average exhaust temperature at the evaporator outlet between the second grid and the third grid systems is 0.31%. Therefore, the solution precision of the third grid system is satisfactory.

Fluent 14.5 is used for the numerical calculation. A finite volume method is employed to discretize the governing equations. The SIMPLE (semi-implicit method for pressure linked equations) algorithm is adopted during the numerical calculation process. A non-slip boundary condition is assumed for all the solid surfaces of the computational domain. The convergence criteria for the velocity and the momentum equations are the residual errors being less than  $10^{-3}$ , convergence criteria for the energy equation is the residual error being less than  $10^{-6}$ .

#### 2.4. Experimental Validation of Evaporator Numerical Simulation

The diesel engine–ORC combined system mainly includes two parts, diesel engine system and ORC system, in the combined system, the diesel cycle (for the diesel engine) is the topping cycle, and the Rankine cycle (for the ORC system) is the bottoming cycle.

The diesel engine experimental system mainly includes the diesel engine, the measurement and control system, the fuel supply system, the cooling system. The turbocharged diesel engine BJ493ZLQ3 used in this research is a four-cylinder and four-stroke vehicle engine equipped with an electronically controlled high-pressure common-rail fuel injection system.

The ORC experimental system is mainly composed of a pump, evaporator, expander, condenser, reservoir, the measurement and control system for expander, the lubrication system for expander, the cooling system and the data acquisition system for ORC system. Figure 3 shows a schematic diagram of the ORC system used in this study.

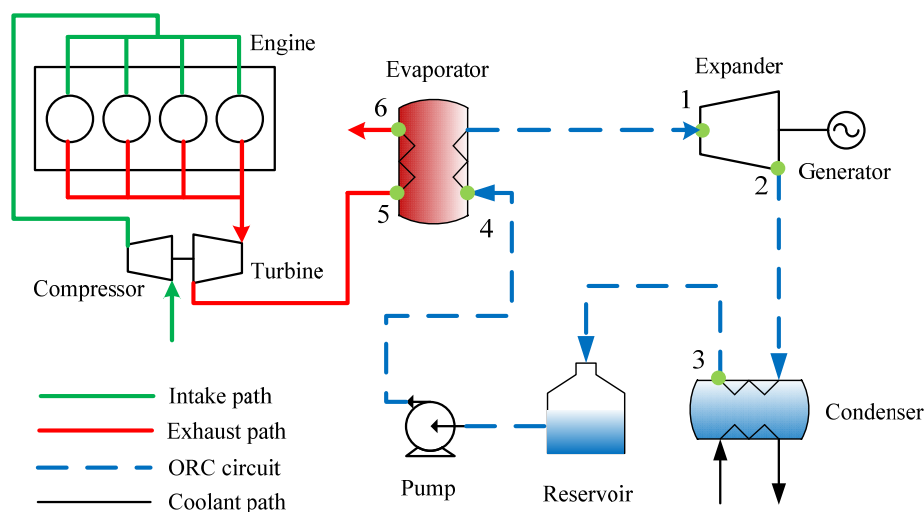


**Figure 3.** Schematic of the organic Rankine Cycle (ORC) system.

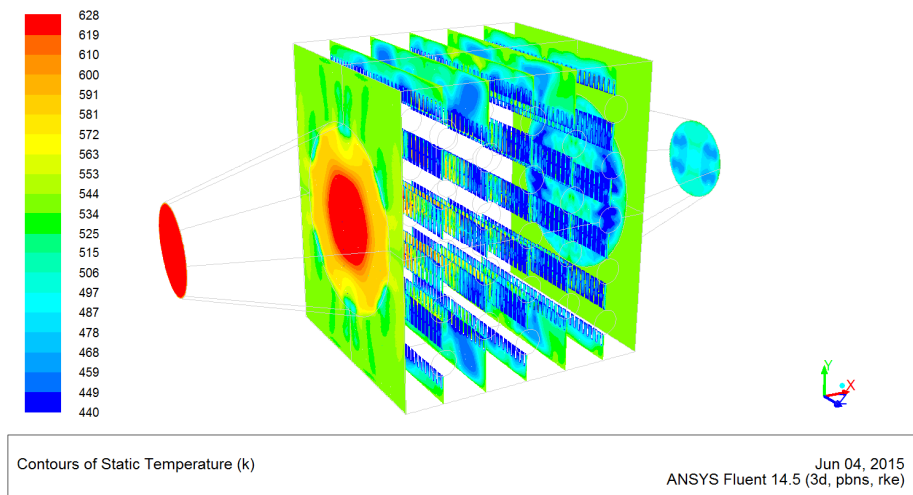
The data acquisition system for ORC system mainly includes the temperature sensors, the pressure sensors, and the flowmeters. The pressure sensors are used for measuring the pressure at the outlet of pump, the outlet of evaporator at the tube side, the outlet of expander, the outlet of condenser. The temperature sensors are used for measuring the temperature at the outlet of pump, the outlet of evaporator at the tube side, the inlet and outlet of the evaporator at the shell side, the outlet of expander, the outlet of condenser. A flowmeter metering the volume flow rate of the working fluid is installed on the pipe between the evaporator and the expander.

During the experiment, the exhaust temperature of the inlet and outlet at the evaporator shell side can be obtained by temperature sensors. Then, we can use the experimental data to validate the numerical simulation results.

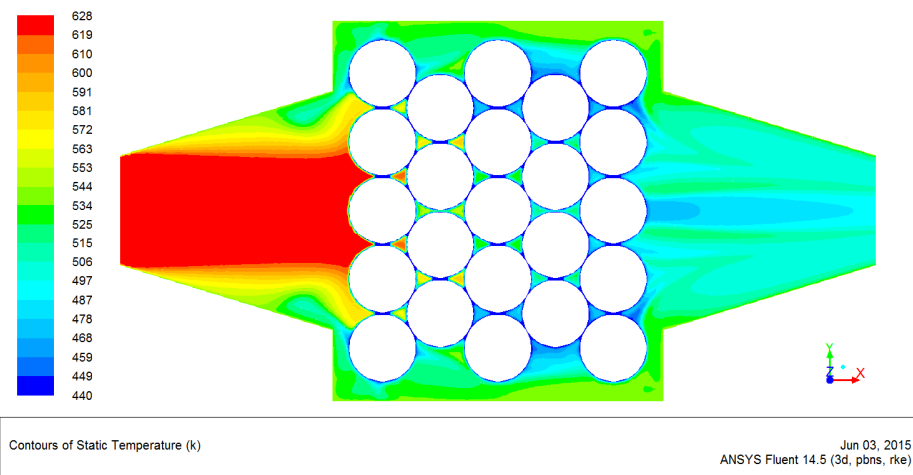
When the engine speed is  $2600 \text{ r}\cdot\text{min}^{-1}$  and the engine torque is  $180.7 \text{ N}\cdot\text{m}$  according to the experiment, the measured temperature at the outlet of the evaporator is  $491 \text{ K}$ . According to the numerical simulation, the average exhaust temperature at the outlet of the evaporator is  $490.5 \text{ K}$ . The relative error of the exhaust temperature at the evaporator outlet between experimental value and simulation value is  $0.1\%$ , which indicates that the numerical simulation correlates well with the actual heat transfer process. During the experiment, several temperature sensors should be installed at the evaporator outlet to obtain the more accurate experimental value, and the average value of the temperature sensors should be taken as the experimental value. In this research, only one temperature sensor is installed at the evaporator outlet, which can lead to higher relative error of the exhaust temperature at the evaporator outlet between the experimental and simulation values. To validate the numerical results more precisely with the experimental data, more values of the static temperatures of the exhaust should be measured at different positions in the evaporator and later compared with the numerical values.

### *2.5. Results and Discussion of the Evaporator Numerical Simulation*

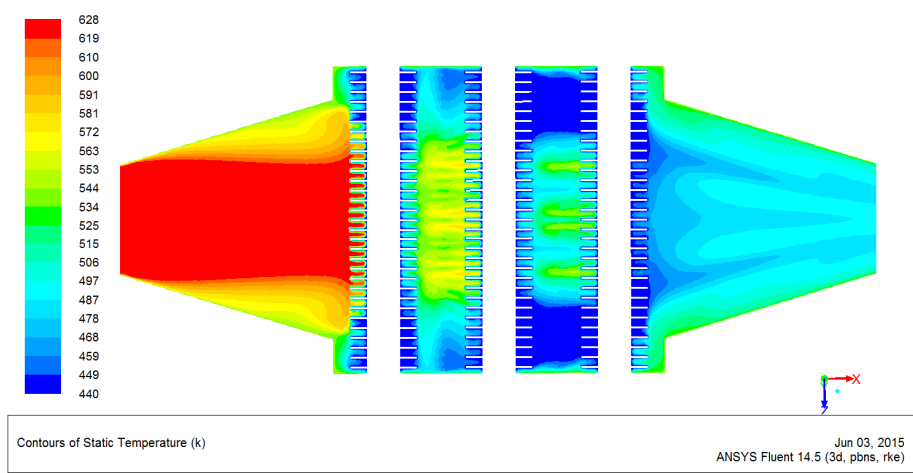
To reduce the calculation workload, a quarter of the physical model of the evaporator is used for the calculations based on the symmetry principle. Afterwards, the calculation results (for a quarter of the physical model of the evaporator) are symmetrized along the symmetric planes perpendicular to the z-axis and the y-axis. Then, the calculation results for the physical model of the evaporator can be obtained. To analyze the flow and heat transfer characteristics of the engine exhaust at the evaporator shell side, nine planes in different positions vertical to the x-axis are selected, which are shown in Figure 4a. The nine planes include the plane of the inlet of the entire flow domain, the plane of the outlet of the entire flow domain, the interface between the front end portion and the main body, the interface between the back end portion and the main body, and the planes through the centerlines of the tube bundles in each row along the direction of the exhaust flow. In addition, the symmetric plane vertical to the z-axis and symmetric plane vertical to the y-axis are selected, which are shown in Figure 4b,c.



(a)



(b)

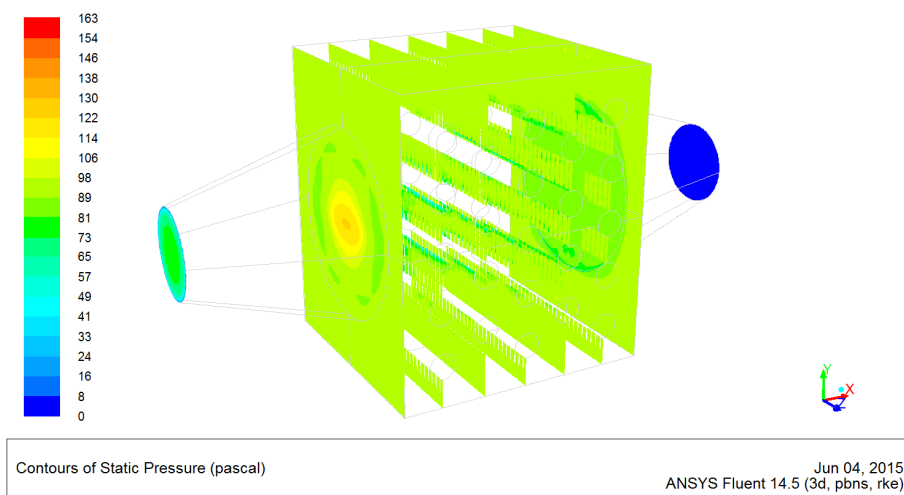


(c)

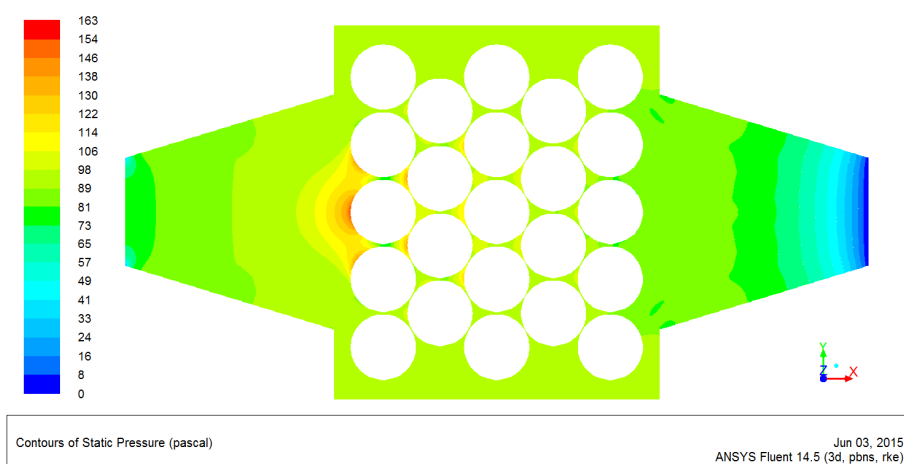
**Figure 4.** Temperature distribution of exhaust in the evaporator. (a) Nine planes in different positions vertical to the x-axis; (b) Symmetric plane vertical to the z-axis; (c) Symmetric plane vertical to the y-axis.

The temperature distribution of the exhaust at the evaporator shell side is shown in Figure 4. The exhaust temperature in the front end portion approximately equals the inlet exhaust temperature of 628 K. In addition, the flow areas of the high temperature exhaust gas are nearly round, and expand gradually along the flow direction. The main reason is that the shape of the front end portion that connects with the main body is round, and the exhaust gas temperatures decrease gradually along the flow direction. The high-temperature exhaust gas in the flow space between the first and second rows diffuses quickly.

The pressure distribution of the exhaust at the evaporator shell side is shown in Figure 5. As shown in Figure 5, the maximum pressure exists in the central areas near the tube bundles of the first row towards the front end portion. The high temperature exhaust in the conical divergent pipe is blocked by the tube bundles of the first row; the exhaust mass flow rate decreases rapidly, then the exhaust pressure increases rapidly. The maximum pressure is about 169 Pa (relative pressure) and is significantly lower than the maximum limit of 30 kPa. The pressure drop of the exhaust gas between the inlet and outlet of the evaporator is about 78 Pa, which is the exhaust back pressure increment at this operating point of the diesel engine.

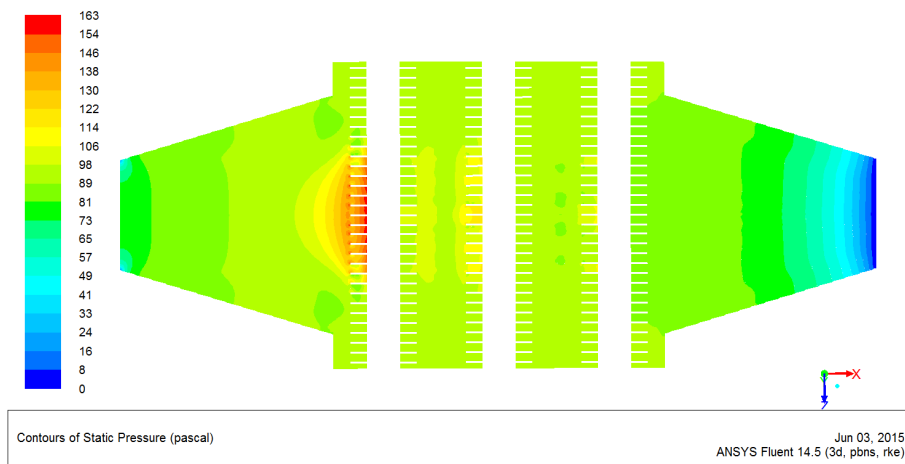


(a)



(b)

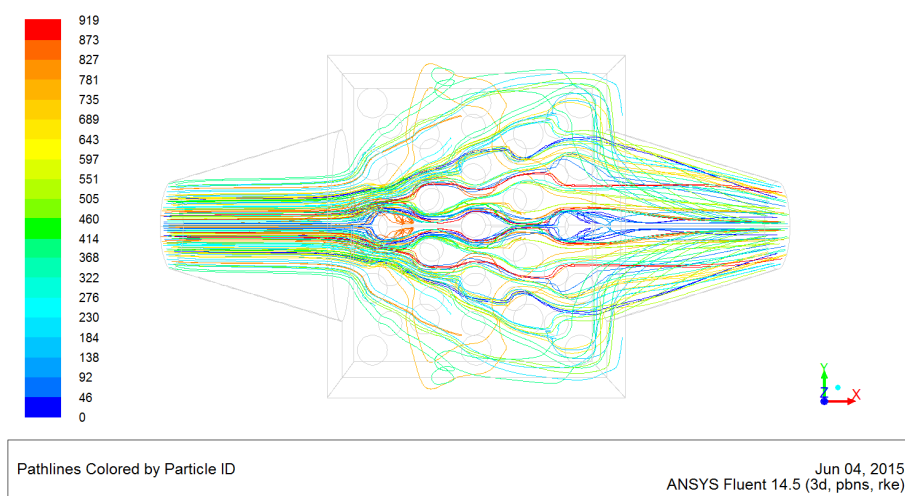
Figure 5. Cont.



(c)

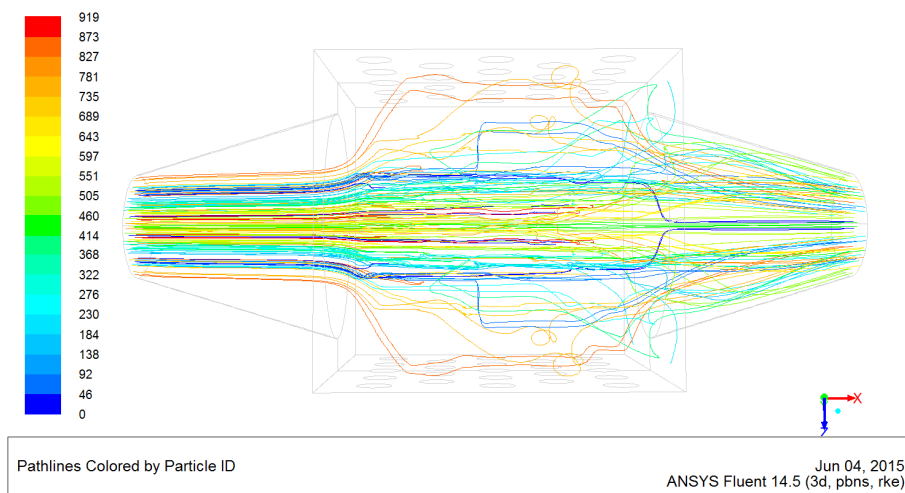
**Figure 5.** Pressure distribution of exhaust in the evaporator. (a) Nine planes in different positions vertical to the x-axis; (b) Symmetric plane vertical to the z-axis; (c) Symmetric plane vertical to the y-axis.

The streamlines of the exhaust gas in the evaporator are shown in Figure 6. Figure 6a is the view in the negative direction of the z-axis. Figure 6b is the view in the negative direction of the y-axis. In the central space of the evaporator, the exhaust flow is well distributed, which means the convective heat transfer is fully developed. In the four corners far from the center of the evaporator and near the front end portion, almost no exhaust flow exists, which means that the convective heat transfer is very weak. The exhaust flow that enters the main body is restricted in the domains close to the central space of the evaporator because the shape of the front end portion that connects with the main body is round. Therefore, to ensure the exhaust flow is evenly distributed in the spaces between the neighboring fin layers, a reasonable design of the shapes that connect the main body with the front end and back end portions is necessary.



(a)

**Figure 6.** Cont.



(b)

**Figure 6.** Streamlines of the exhaust gas in the evaporator. (a) The view in the negative direction of the z-axis; (b) The view in the negative direction of the y-axis.

To improve the heat transfer performance of the fin-and-tube evaporator from the viewpoint of the field synergy principle, the field synergy angle between the velocity and the temperature gradient in the flow field is discussed. The field synergy principle is different from the traditional heat transfer enhancement theory [29–31]. According to the field synergy principle, the convective heat transfer performance not only depends on the velocity of the fluid, the thermodynamic properties of the fluid, and the temperature difference between the fluid and solid wall, but also on the situation of synergy between the velocity field and the temperature gradient field.

For a steady, 2D boundary layer flow over a cold flat plate at zero incident angle, as shown in Figure 7a. The energy equation is:

$$\rho c_p \left( u \frac{\partial T}{\partial x} + v \frac{\partial T}{\partial y} \right) = \frac{\partial}{\partial y} \left( \lambda \frac{\partial T}{\partial y} \right) \tag{7}$$

The energy equation for conduction with the heat source between two parallel plates at constant but different temperatures as shown in Figure 7b is:

$$-\dot{q} = \frac{\partial}{\partial y} \left( \lambda \frac{\partial T}{\partial y} \right) \tag{8}$$

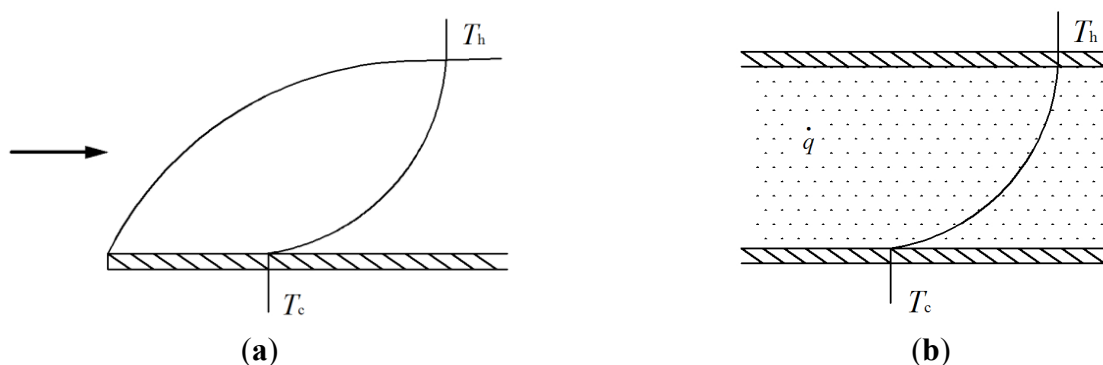


**Figure 7.** Temperature profiles. (a) Laminar boundary layer; (b) Conduction with a heat source.

From Equations (7) and (8) and Figure 7, it can be seen that the convection term in the energy equation for the boundary layer flow corresponds to the heat source term in the conduction equation. The presence of heat sources leads to increased heat flow at the boundary for both the conduction and convection problems. The integral of Equation (7) over the thickness of the thermal boundary layer is:

$$\int_0^{\delta_t, R} \rho c_p \left( u \frac{\partial T}{\partial x} + v \frac{\partial T}{\partial y} \right) dy = -\lambda \left. \frac{\partial T}{\partial y} \right|_w \quad (9)$$

From Equation (9), we can see that the wall heat flow is equal to the overall strength of the heat sources inside the thermal boundary layer. This means that the convection heat transfer can be enhanced by increasing the quantity of the integral of the convection terms over the thermal boundary layer. Equation (9) can be rewritten with the convection term in vector form as:

$$\int_0^{\delta_t, R} \rho c_p (\mathbf{U} \cdot \nabla T) dy = -\lambda \left. \frac{\partial T}{\partial y} \right|_w \quad (10)$$

According to Equation (10), for a certain flow rate and temperature difference between the wall and the incoming flow, the wall heat flow increases with the decrease of the included intersection angle between the velocity and temperature gradient.

With the following dimensionless variables for the boundary layer flow:

$$\bar{U} = \frac{U}{U_\infty}, \quad \nabla \bar{T} = \frac{\nabla T}{(T_\infty - T_w) / \delta_t}, \quad \bar{y} = \frac{y}{\delta_t}, \quad T_\infty > T_w \quad (11)$$

Equation (10) can be written in the dimensionless form:

$$Nu_x = Re_x Pr \int_0^1 (\bar{U} \cdot \nabla \bar{T}) d\bar{y} \quad (12)$$

From Equation (12), it can be seen that there are two ways to enhance heat transfer: (a) increasing Reynolds or/and Prandtl number; which is well known in the literature; (b) increasing the value of the dimensionless integration.

The vector dot product,  $\bar{U} \cdot \nabla \bar{T}$  in the dimensionless integration in Equation (12) can be expressed as:

$$\bar{U} \cdot \nabla \bar{T} = |\bar{U}| \cdot |\nabla \bar{T}| \cos \beta \quad (13)$$

$\beta$  is the field synergy angle. The field synergy angle is the intersection angle between the velocity vector and the temperature gradient.

Deduced from Equation (12) is:

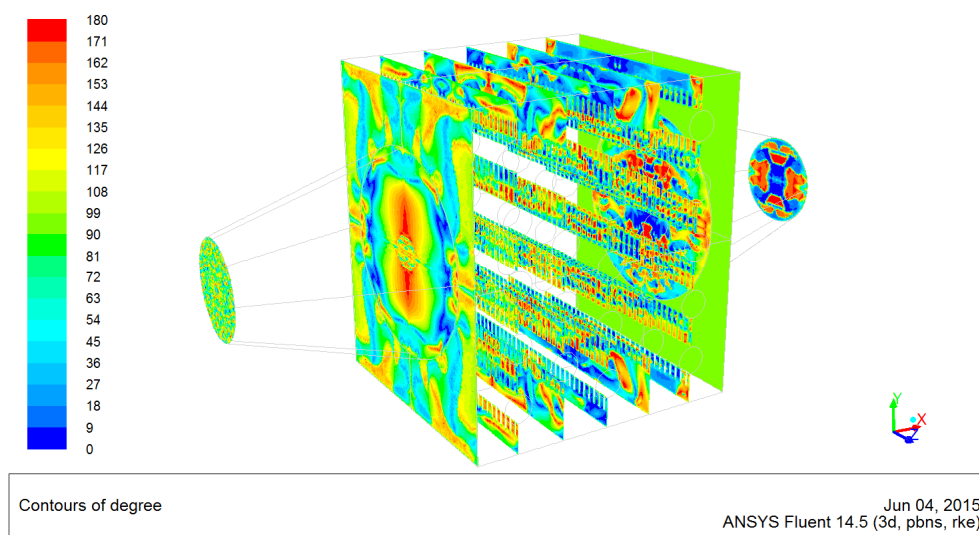
$$St = \frac{Nu}{Re_x Pr} = I \quad (14)$$

$$I = \int_0^1 (\bar{U} \cdot \nabla \bar{T}) d\bar{y} \quad (15)$$

$$I = f(Re_x, Pr) \quad (16)$$

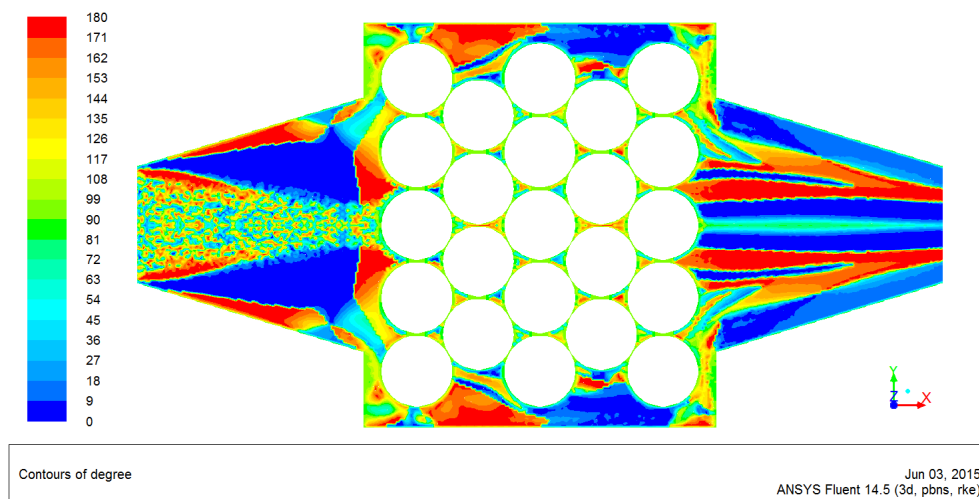
According to the abovementioned equations, we can see that convective heat transfer performance is significantly relative to the situation of synergy between the velocity field and the temperature gradient field. From the point of view of scalar, the synergy between the velocity field and the temperature gradient field is the synergy among the absolute value of velocity, the absolute value of temperature gradient, and the cosine of the intersection angle between the velocity vector and the temperature gradient ( $\beta$ , field synergy angle). When the absolute values of velocity and temperature gradient are constant and  $\beta < 90^\circ$ ,  $I$  increases with the decrease of the  $\beta$ . Thus,  $Nu$  increases and heat transfer enhancement can be achieved. When the absolute values of velocity and temperature gradient are constant and  $\beta > 90^\circ$ ,  $I$  increases with the increase of the  $\beta$ . Thus,  $Nu$  increases and heat transfer enhancement can be achieved. Thus, coordinating the velocity field and the temperature gradient field is a novel way for heat transfer enhancement.

Previously, we studied the synergy situation of a fin-and-tube evaporator [32]. However, in that study, although the velocity vectors and the temperature gradient vectors were obtained, detailed synergy angles were not determined. In this study, a program is developed in CFD-post software to calculate the synergy angles at various positions of the evaporator shell side. The calculation results are shown in Figure 8. The synergy angle distribution for nine planes in different positions vertical to the x-axis is shown in Figure 8a. The synergy angle distribution for the symmetric plane vertical to the z-axis and y-axis is shown in Figures 8b and 8c, respectively. The blue and red areas in Figure 8 represent the synergy angles between the velocity and temperature gradient are  $0^\circ$  and  $180^\circ$ , respectively. Correspondingly, the effect of the field synergy between the velocity and the temperature gradient is satisfactory, then heat transfer enhancement can be achieved. The green area in Figure 8 represents the synergy angle between the velocity and temperature gradient is  $90^\circ$ , where the field synergy between the velocity and temperature gradient is weak.

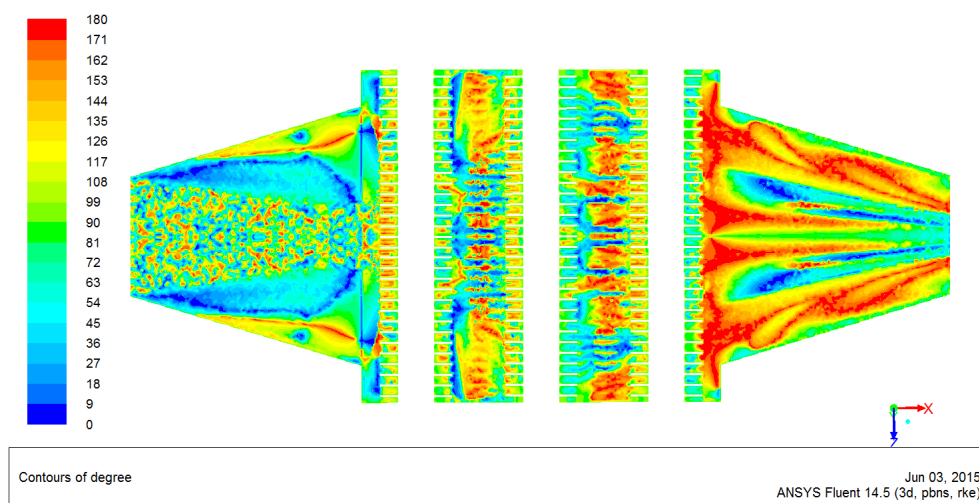


(a)

Figure 8. Cont.



(b)



(c)

**Figure 8.** Synergy angle distribution of exhaust in the evaporator. (a) Nine planes in different positions vertical to the x-axis; (b) Symmetric plane vertical to the z-axis; (c) Symmetric plane vertical to the y-axis.

As we can see from Figure 8, the synergy angle between the velocity and temperature gradient are close to the blue or red color ( $0^\circ$  or  $180^\circ$ ) in the areas among the tube bundles of the evaporator main body. Thus, the field synergy effect for these areas is satisfactory. The synergy angle between the velocity and the temperature gradient is close to the red ( $180^\circ$ ) in the areas among the fins on the windward side. Thus, the field synergy effect for these areas is satisfactory. However, the synergy angle is close to the green ( $90^\circ$ ) in the areas among the fins on the leeward side. Thus, the field synergy effect for these areas is weak. The temperature gradients in the areas close to the fins are nearly vertical to the surface of the fins, which is also vertical to the flow direction of the exhaust, because of the relatively large external diameters of the fins and the heat conduction effects. To further improve heat transfer performance, the layout of the fins can be modified, and the shapes and angles of the fins can be adjusted to make the synergy angle between the velocity and the temperature gradient close to  $0^\circ$  or  $180^\circ$ .

### 3. Numerical Simulation for Diesel Engine

#### 3.1. Simulation Model of Diesel Engine

In this research, the turbocharged diesel engine BJ493ZLQ3 is a four-cylinder and four-stroke vehicle engine equipped with an electronically controlled high-pressure common-rail fuel injection system. The simulation model for BJ493ZLQ3 diesel engine is built by using GT–Power software, which is shown in Figure 9. The simulation model mainly includes an air intake system, four fuel injectors, four cylinders, a crankcase, a turbocharger, and an exhaust system. The main technical parameters of the BJ493ZLQ3 diesel engine are listed in Table 4.

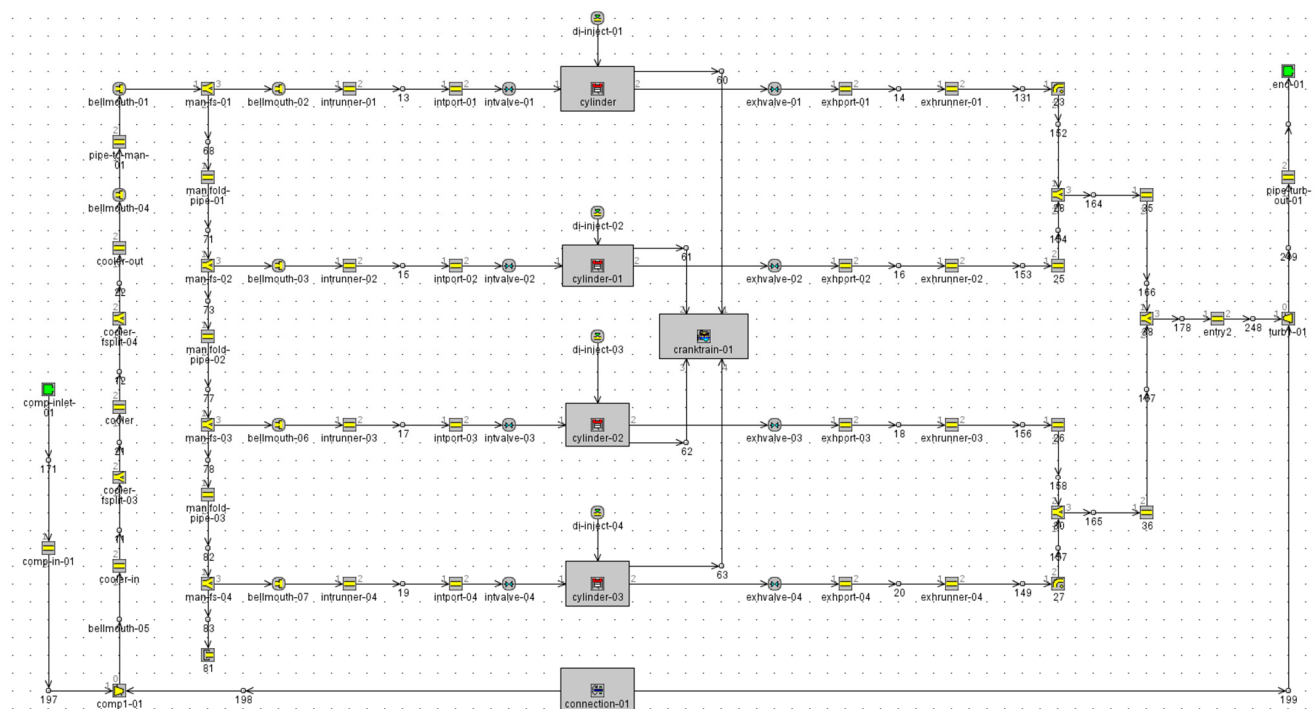


Figure 9. Simulation model of BJ493ZLQ3 diesel engine.

Table 4. Technical parameters of the BJ493ZLQ3 diesel engine.

Item	Parameter	Unit
Type	turbocharged common-rail diesel engine	-
Cylinder diameter	93	mm
Stroke	102	mm
Compression ratio	17.4	-
Displacement	2.771	L
Rated power	85	kW
Rated speed	3600	r·min <sup>-1</sup>
Maximum torque	280	N·m
Speed at max. torque	2300	r·min <sup>-1</sup>

### 3.2. Validation of Diesel Engine Simulation Model

In order to ensure that the simulation model can accurately describe the actual operation of the diesel engine and effectively predict the performance of the diesel engine, the simulation results for various operating points are verified by using the test data of BJ493ZLQ3 diesel engine.

The simulation and experiment results of engine power at full load are shown in Figure 10. Simulation results have the same variation trend with experiment results. When the diesel engine speed is  $3400 \text{ r}\cdot\text{min}^{-1}$ , the relative error between the simulation and experiment values of the engine power reaches its maximum of approximately 4.55%.

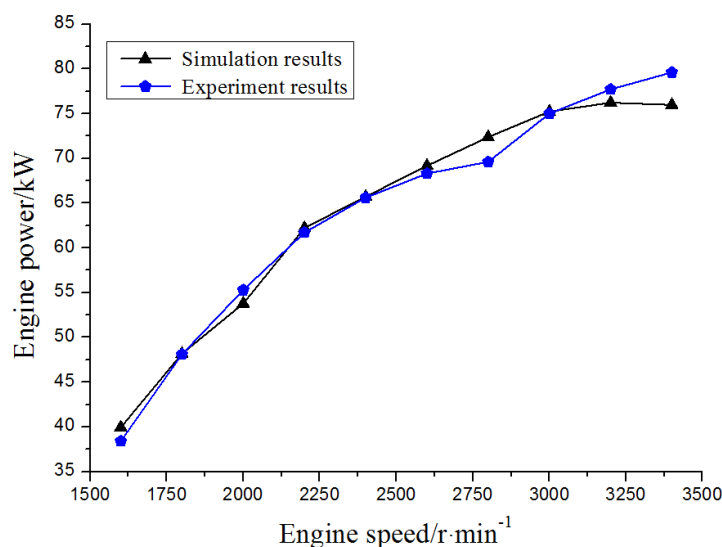


**Figure 10.** Simulation and experiment results of engine power at full load.

The simulation and experiment results of the engine torque at full load are shown in Figure 11. Simulation results have the same variation trend with experiment results. When the diesel engine speed is  $3400 \text{ r}\cdot\text{min}^{-1}$ , the relative error between the simulation and experiment values of the engine torque reaches its maximum of approximately 4.65%.

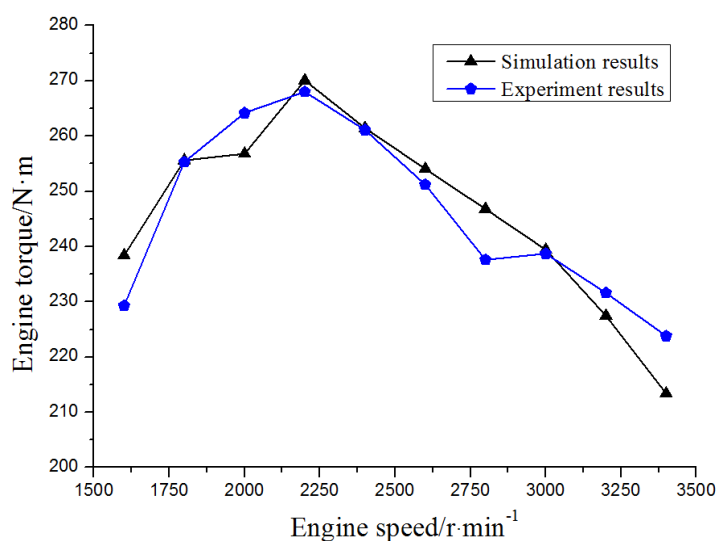


**Figure 11.** Simulation and experiment results of engine torque at full load.

The simulation and experiment results of the BSFC of BJ493ZLQ3 diesel engine at full load are shown in Figure 12. Simulation results have the same variation trend with experiment results. When the diesel engine speed is  $3400 \text{ r}\cdot\text{min}^{-1}$ , the relative error between the simulation and experiment values of the BSFC reaches its maximum of approximately 4.97%.

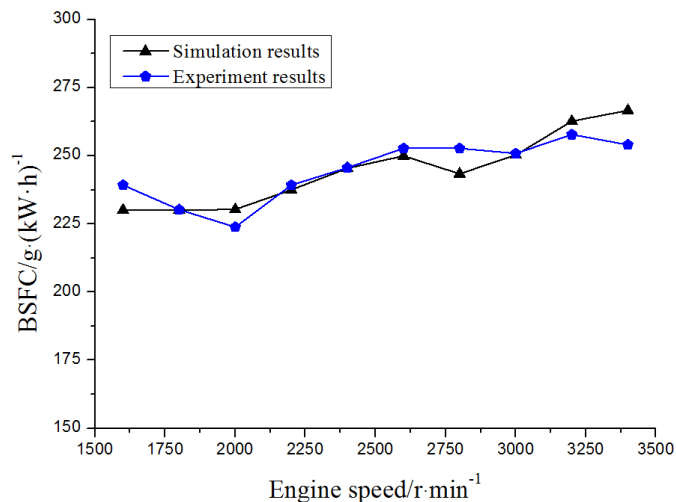


**Figure 12.** Simulation and experiment results of brake specific fuel consumption (BSFC) at full load.

According to the abovementioned analysis, the maximum relative error between the simulation and the experiment values is less than 5%. Therefore, it can be concluded that the engine simulation model can be employed with high precision.

#### 4. Analysis of the Operating Performance for Diesel Engine–ORC Combined System

##### 4.1. Influence of Pressure Drop of Evaporator on the Engine Operating Characteristics

In this study, the influence of the pressure drop of the evaporator of the ORC system on engine operating characteristics is analyzed for 14 different operating points at full load (the engine speed is selected as 1000, 1200, 1400, 1600, 1800, 2000, 2200, 2400, 2600, 2800, 3000, 3200, 3400, and  $3600 \text{ r}\cdot\text{min}^{-1}$ , respectively). According to the pressure drop between the inlet and the outlet of the evaporator based on numerical simulation results of the evaporator, the exhaust back pressure increment of the diesel engine is obtained. When the diesel engine is combined with the ORC system, the diesel engine–ORC combined system is established, which is beneficial in improving fuel economy and power performance. Considering the diesel engine–ORC combined system, the variation of the engine power, engine torque, and BSFC is discussed under various operating points by the simulation based on GT–Power software.

The exhaust back pressure increment of the diesel engine at full load with consideration of the diesel engine–ORC combined system is shown in Figure 13. With the increase of engine speed, the exhaust back pressure increment increases gradually because the intake air mass flow rate of the diesel engine gradually increases with the increase of the engine speed, which results in the increase of the engine exhaust mass flow rate. The pressure drop of the engine exhaust increases at the evaporator shell side.

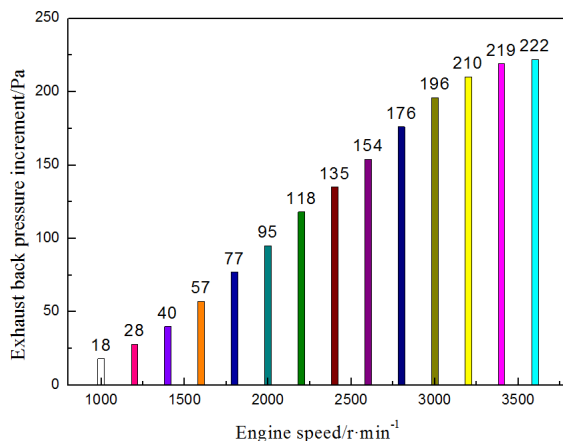


**Figure 13.** Exhaust back pressure increment of diesel engine at full load.

With consideration of the diesel engine–ORC combined system, the power loss, the torque loss, and the BSFC increment of the diesel engine are discussed under various operating points and shown in Figures 14–16. Both the engine power and torque decrease, with a maximum decrease of less than 1%. The BSFC increases with a maximum increase of less than 1% because the flow resistance of the engine exhaust on the evaporator shell side exists, thereby increasing the exhaust back pressure of the diesel engine.

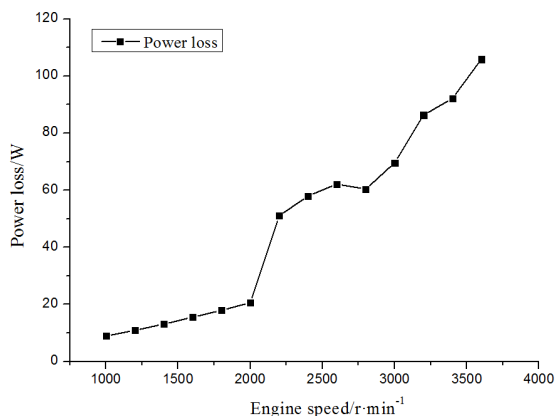


**Figure 14.** Power loss of diesel engine at full load.

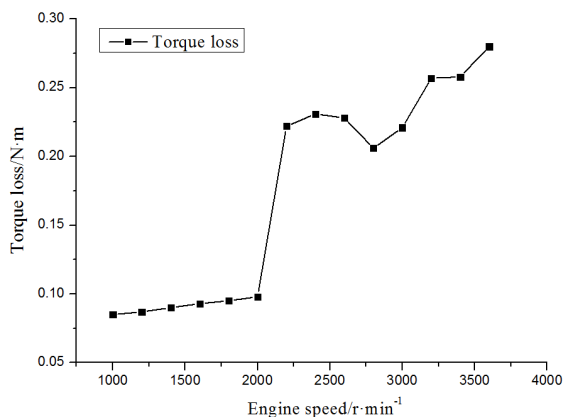


**Figure 15.** Torque loss of diesel engine at full load.

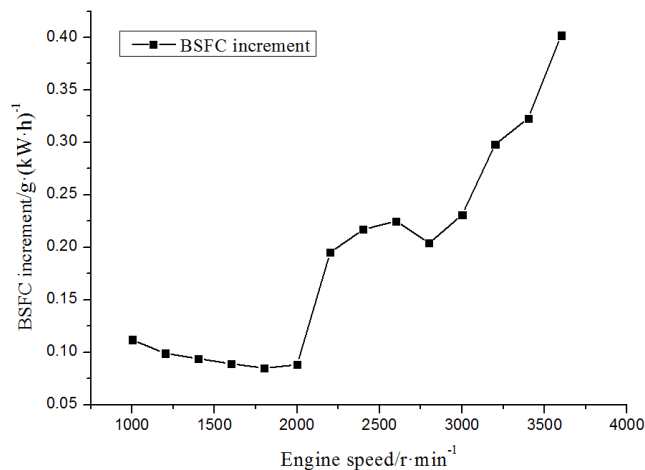


**Figure 16.** BSFC increment of diesel engine at full load.

#### 4.2. Thermodynamic Model of the ORC System

The  $T$ - $s$  diagram of the ORC system is shown in Figure 17. The ORC system comprises a pump, an evaporator, an expander, a condenser, and a reservoir. Process 5–6 is the heat rejection process of the diesel engine exhaust at the evaporator shell side. Process 1–2 is the actual expansion process, whereas Process 1–2s is the isentropic expansion process in which the working fluid soon turns into low-temperature and low-pressure gas. At the same time, the expander produces useful work used to generate electricity. Process 2–3 is the constant pressure heat rejection process, in which the working fluid turns into liquid in the condenser and flows into the reservoir. Process 3–4 is the actual compression process, whereas Process 3–4s is the isentropic compression process in which the working fluid is pressurized into high-pressure liquid state by using a pump. Process 4–1 is the constant pressure heat addition process in which the working fluid absorbs the heat from the engine exhaust in the evaporator and soon turns into high-temperature and high-pressure gas.

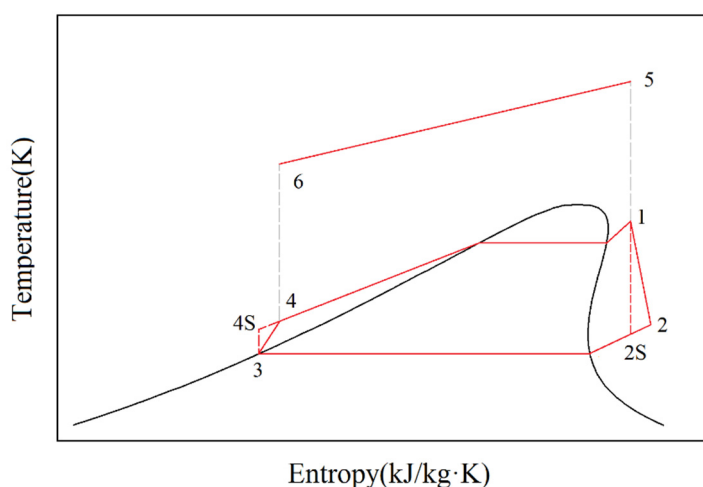


**Figure 17.**  $T$ - $s$  diagram of the ORC system.

The power output of the expander  $\dot{W}_s$  can be calculated as follows:

$$\dot{W}_s = \dot{m}(h_1 - h_2)\eta_s \quad (17)$$

The heat transfer rate of the condenser  $\dot{Q}_c$  can be calculated as follows:

$$\dot{Q}_c = \dot{m}(h_2 - h_3) \quad (18)$$

The power consumed by pump  $\dot{W}_p$  can be calculated as follows:

$$\dot{W}_p = \dot{m}(h_4 - h_3) = \dot{m}(h_{4s} - h_3) / \eta_p \quad (19)$$

The heat transfer rate of the evaporator  $\dot{Q}_e$  can be calculated as follows:

$$\dot{Q}_e = \dot{m}(h_1 - h_4) \quad (20)$$

The net power output of ORC system  $\dot{W}_n$  can be calculated as follows:

$$\dot{W}_n = \dot{W}_s - \dot{W}_p \quad (21)$$

In this study, the following assumptions are made for the ORC system:

- (1) The pressure drop and heat loss in each component as well as pipelines are neglected.
- (2) The evaporation pressure ranges from 1.0 MPa to 3.5 MPa.
- (3) The ambient temperature is set to 293 K.
- (4) The expansion ratio of the expander is limited to 8.
- (5) The working fluid releases heat in the condenser and then turns into saturated liquid.
- (6) The isentropic efficiencies of the expander and the pump are both set to 0.8.

To evaluate the performance of the diesel engine–ORC combined system, the power increase rate of the diesel engine–ORC combined system can be expressed as

$$\eta_w = \frac{\dot{W}_n + \dot{W}_b - \dot{W}_i}{\dot{W}_i} \times 100\% \quad (22)$$

The BSFC of the diesel engine–ORC combined system can be expressed as

$$bsfc_{com} = \frac{\dot{m}_{fuel}}{\dot{W}_n + \dot{W}_b} \times 3.6 \times 10^6 \quad (23)$$

The BSFC decrease rate of the diesel engine–ORC combined system can be expressed as

$$\eta_{bsfc} = \frac{bsfc - bsfc_{com}}{bsfc} \times 100\% \quad (24)$$

#### 4.3. Operating Performance of Diesel Engine–ORC Combined System

In this research, R245fa is selected as the working fluid. Figure 18 shows the variation of the power increase rate of the diesel engine–ORC combined when the evaporation pressure ranges from 1.0 MPa to 3.5 MPa for the 14 operating points at full load of the diesel engine. The variation of the BSFC decrease rate of the diesel engine–ORC combined system is shown in Figure 19.

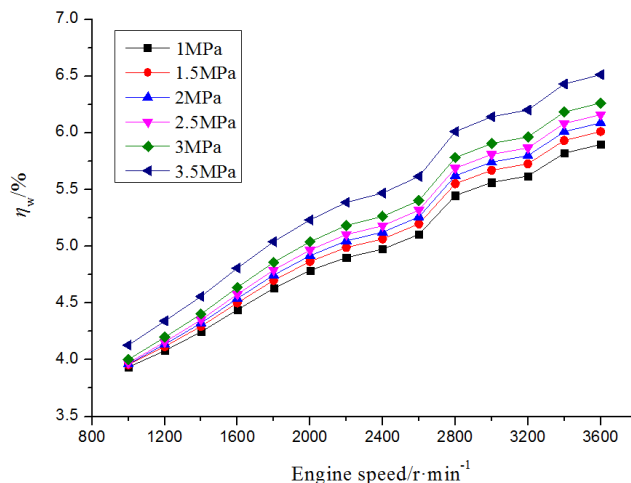


**Figure 18.** Variation of  $\eta_w$  with engine speed and evaporation pressure.

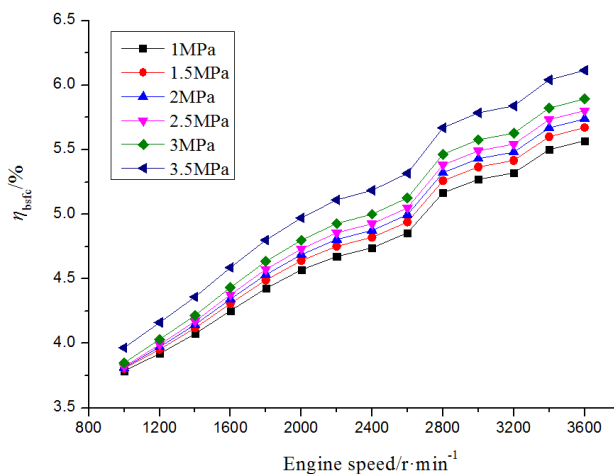


**Figure 19.** Variation of  $\eta_{bsfc}$  with engine speed and evaporation pressure.

As shown in Figure 18, when the engine speed is kept constant, the power increase rate of the diesel engine–ORC combined system gradually increases with the increase of evaporation pressure. The main reason is that, on the one hand, the net power output of the ORC system increases with the increase of evaporation pressure. On the other hand, the power loss of diesel engine caused by the pressure drop of the engine exhaust at the evaporator shell side is far lower than the former. When the evaporation pressure is kept constant, the power output of the diesel engine–ORC combined system gradually increases with the increase of engine speed. The main reason for this condition is that with the increase of engine speed, on one hand, the available exhaust energy from the diesel engine increases, then the net power output of the ORC system increases. On the other hand, the power loss of diesel engine caused by the pressure drop of engine exhaust at the evaporator shell side also increases, which is far lower than the former. The maximum value of the power increase rate of the diesel engine–ORC combined system is 6.5%.

As shown in Figure 19, when the engine speed is kept constant, the BSFC decrease rate of the diesel engine–ORC combined system gradually increases with the increase of evaporation pressure. When the evaporation pressure is kept constant, the BSFC decrease rate of the diesel engine–ORC combined system gradually increases with the increase of engine speed. The maximum value of the BSFC decrease rate of the diesel engine–ORC combined system is 6.1%.

## 5. Conclusions

In this paper, a CFD model of a fin-and-tube evaporator of an ORC system is established by using Fluent software. The flow and heat transfer characteristics of the engine exhaust at the evaporator shell side are obtained. The performance of the fin-and-tube evaporator is analyzed based on the field synergy principle. A simulation model of the diesel engine is built based on GT–Power under various operating conditions. The influence of the pressure drop of the engine exhaust at the evaporator shell side on diesel engine performance is studied. The variation tendency of the power output and BSFC of diesel engine–ORC combined system are discussed.

- (1) The exhaust gas temperatures decrease gradually along the flow direction at the evaporator shell side. The high-temperature exhaust gas in the flow space between the first and second rows diffuses quickly. To ensure that the exhaust flow is evenly distributed in the spaces between the neighboring fin layers, a reasonable design of the shapes that connect the main body with the front end and back end portions is necessary.
- (2) The field synergy effect for the areas among the tube bundles of the evaporator main body and the field synergy effect for the areas among the fins on the windward side are satisfactory. However, the field synergy effect for the areas among the fins on the leeward side is weak. To further improve the heat transfer performance, the layout of the fins can be modified, and the shapes and angles of the fins can be adjusted to make the synergy angle between the velocity and the temperature gradient close to  $0^\circ$  or  $180^\circ$ , which can provide a theoretical guide for the design and performance optimization of the fin-and-tube evaporator.
- (3) As a result of the pressure drop caused by the evaporator of the ORC system, the diesel engine power and torque decrease slightly, whereas the BSFC increases slightly with the increase of the exhaust back pressure. With the increase of engine speed, the power loss, the torque loss, and the BSFC increment increase gradually, with the most significant change being less than 1%.
- (4) Compared with the diesel engine itself, the maximum increase of power output is 6.5% for the diesel engine–ORC combined system, and the maximum decrease of BSFC is 6.1%.

In this research, we have done some experimental and simulation work for the existing evaporator of ORC system in our laboratory. In the near future, the heat transfer performance of the evaporator and the influence of pressure drop on the operating characteristics of the diesel engine–ORC combined system will be discussed for different kinds of evaporators. To further improve the heat transfer performance of the evaporator and the operating performance of the diesel engine–ORC combined system, the flow and heat transfer characteristics of the working fluid at the evaporator tube side should be investigated.

## Acknowledgments

This work was sponsored by the National Natural Science Foundation of China (Grant No. 51376011), the Beijing Natural Science Foundation Program (Grant No. 3152005), the Scientific Research Key Program of Beijing Municipal Commission of Education (Grant No. KZ201410005003), the National Basic Research Program of China (973 Program) (Grant No. 2011CB707202), and the Key Project of Thirteenth Scientific Research Foundation for Graduate Students in Beijing University of Technology (Grant No. ykj-2014-10708).

## Author Contributions

Chen Bei wrote the main body of the paper. Hongguang Zhang and Fubin Yang revised the paper. Songsong Song, Enhua Wang, and Hao Liu performed the simulations. Ying Chang, Hongjin Wang, and Kai Yang performed the experiments. All authors read and approved the manuscript.

## Conflicts of Interest

The authors declare no conflict of interests.

## Acronyms

ORC	organic Rankine cycle
BSFC	brake specific fuel consumption

## Greek Letters

$\rho$	density ( $\text{kg}\cdot\text{m}^{-3}$ )
$\lambda$	thermal conductivity ( $\text{W}\cdot(\text{m}\cdot\text{K})^{-1}$ )
$\mu$	dynamic viscosity ( $\text{kg}\cdot(\text{m}\cdot\text{s})^{-1}$ )
$\Phi_a$	excess air coefficient
$\Phi_{ij}$	interaction factor
$\eta_w$	power increase rate of the diesel engine-ORC combined system (%)
$\eta_{\text{bsfc}}$	BSFC decrease rate of the diesel engine-ORC combined system (%)
$\delta_t$	thermal boundary layer thickness (m)
$\beta$	intersection angle between velocity and temperature gradient (degree)
$\eta_p$	isentropic efficiency of pump (%)
$\eta_s$	isentropic efficiency of expander (%)

## Subscripts

1, 2, 2s, 3, 4, 4s, 5, 6	state points in cycle (see Figure 17)
comb	diesel engine-ORC combined system
s	expander
p	pump
e	evaporator
c	condenser
n	net
m	average
w	value on the wall surface
x	based on length x

## Nomenclature

$c_p$	specific heat at constant pressure ( $\text{J}\cdot(\text{kg}\cdot\text{K})^{-1}$ )
$M$	molecular weight ( $\text{kg}\cdot\text{kmol}^{-1}$ )
$mf$	mass fraction
$\nu_f$	mole fraction

$x, y$	Cartesian coordinates (m)
$u$	velocity component in x-direction ( $\text{m}\cdot\text{s}^{-1}$ )
$v$	velocity component in y-direction ( $\text{m}\cdot\text{s}^{-1}$ )
$T$	temperature (K)
$\dot{q}$	strength of heat source (kJ)
$R$	radius of the channel (m)
$Re$	Reynolds number
$Pr$	Prandtl number
$Nu$	Nusselt number
$St$	Stanton number
$I$	integral
$U$	velocity ( $\text{m}\cdot\text{s}^{-1}$ )
$\bar{U}$	dimensionless velocity vector
$U_\infty$	free-stream fluid velocity ( $\text{m}\cdot\text{s}^{-1}$ )
$T_\infty$	free-stream fluid temperature (K)
$T_w$	wall temperature (K)
$\nabla T$	temperature gradient ( $\text{K}\cdot\text{m}^{-1}$ )
$\nabla \bar{T}$	dimensionless temperature gradient
$\bar{y}$	dimensionless Cartesian coordinates
$\dot{W}_n$	net power output of ORC system (kW)
$\dot{W}_i$	power output of the diesel engine (kW)
$\dot{W}_b$	power output of the diesel engine in the diesel engine-ORC combined system (kW)
$\dot{m}$	mass flow rate ( $\text{kg}\cdot\text{s}^{-1}$ )
$\dot{W}$	power (kW)
$\dot{Q}$	heat transfer rate (kW)
$bsfc$	BSFC of the diesel engine ( $\text{g}\cdot(\text{kW}\cdot\text{h})^{-1}$ )
$bsfc_{\text{com}}$	BSFC of the diesel engine-ORC combined system ( $\text{g}\cdot(\text{kW}\cdot\text{h})^{-1}$ )
$h$	enthalpy ( $\text{kJ}\cdot\text{kg}^{-1}$ )

## References

1. Dolz, V.; Novella, R.; García, A.; Sánchez, J. HD Diesel Engine Equipped with a bottoming Rankine Cycle as a Waste Heat Recovery System Part I: Study and Analysis of the Waste Heat Energy. *Appl. Therm. Eng.* **2012**, *36*, 269–278.
2. Heywood, J.B. *Internal Combustion Engine Fundamentals*; McGraw-Hill, Inc.: New York, NY, USA, 1988.
3. Kaska, O. Energy and exergy analysis of an organic Rankine for power generation from waste heat recovery in steel industry. *Energy Convers. Manag.* **2014**, *77*, 108–117.
4. Karellas, S.; Leontaritis, A.D.; Panousis, G.; Bellos, E.; Kakaras, E. Energetic and exergetic analysis of waste heat recovery systems in the cement industry. *Energy* **2013**, *58*, 147–156.
5. Wang, J.F.; Yan, Z.Q.; Zhao, P.; Dai, Y.P. Off-design performance analysis of a solar-powered organic Rankine cycle. *Energy Convers. Manag.* **2014**, *80*, 150–157.
6. Uris, M.; Linares, J.I.; Arenas, E. Techno-economic feasibility assessment of a biomass cogeneration plant based on an Organic Rankine Cycle. *Renew. Energy* **2014**, *66*, 707–713.

7. Uusitalo, A.; Honkatukia, J.; Turunen-Saaresti, T.; Larjola, J. A thermodynamic analysis of waste heat recovery from reciprocating engine power plants by means of organic Rankine cycles. *Appl. Therm. Eng.* **2014**, *70*, 33–41.
8. Leslie, N.P.; Zimron, O.; Sweetser, R.S.; Stovall, T.K. Recovered energy generation using an organic Rankine cycle system. *ASHRAE Trans.* **2009**, *115*, 220–230.
9. Imran, M.; Usman, M.; Park, B.S.; Kim, H.J.; Lee, D.H. Multi-objective optimization of evaporator of organic Rankine cycle (ORC) for low temperature geothermal heat source. *Appl. Therm. Eng.* **2015**, *80*, 1–9.
10. Zhang, H.G.; Wang, E.H.; Fan, B.Y. Heat transfer analysis of a finned-tube evaporator for engine exhaust heat recovery. *Energy Convers. Manag.* **2013**, *65*, 438–447.
11. Kundu, B.; Das, P.K. Performance and optimum dimensions of flat fins for tube-and-fin heat exchangers: A generalized analysis. *Int. J. Heat Fluid Flow* **2009**, *30*, 658–668.
12. Zhang, Z.G.; Ma, D.B.; Fang, X.M. Experimental and numerical heat transfer in a helically baffled heat exchanger combined with one three-dimensional finned tube. *Chem. Eng. Process.* **2008**, *47*, 1738–1743.
13. Ozden, E.; Tari, I. Shell side CFD analysis of a small shell-and-tube heat exchanger. *Energy Convers. Manag.* **2010**, *51*, 1004–1014.
14. Zhang, J.F.; Li, B.; Huang, W.J.; Lei, Y.G.; He, Y.L.; Tao, W.Q. Experimental performance comparison of shell-side heat transfer for shell-and-tube heat exchangers with middle-overlapped helical baffles and segmental baffles. *Chem. Eng. Sci.* **2009**, *64*, 1643–1653.
15. An, C.S.; Choi, D.H. Analysis of heat-transfer performance of cross-flow fin-tube heat exchangers under dry and wet conditions. *Int. J. Heat Mass Transf.* **2012**, *55*, 1496–1504.
16. Bhuiyan, A.A.; Amin, M.R.; Sadrul Islam, A.K.M. Three-dimensional performance analysis of plain fin tube heat exchangers in transitional regime. *Appl. Therm. Eng.* **2013**, *50*, 445–454.
17. Tang, L.H.; Zeng, M.; Wang, Q.W. Experimental and numerical investigation on air-side performance of fin-and-tube heat exchangers with various fin patterns. *Exp. Therm. Fluid Sci.* **2009**, *33*, 818–827.
18. Aytunc, E.; Bails, O.; Levent, B. Effect of geometrical parameters on heat transfer and pressure drop characteristics of plate fin and tube heat exchangers. *Appl. Therm. Eng.* **2005**, *25*, 2421–2431.
19. Şahin, H.M.; Dal, A.R.; Baysal, E. 3-D Numerical study on the correlation between variable inclined fin angles and thermal behavior in plate fin-tube heat exchanger. *Appl. Therm. Eng.* **2007**, *27*, 1806–1816.
20. Han, H.; He, Y.L.; Li, Y.S.; Wang, Y.; Wu, M. A numerical study on compact enhanced fin-and-tube heat exchangers with oval and circular tube configurations. *Int. J. Heat Mass Transf.* **2013**, *65*, 686–695.
21. Tao, Y.B.; He, Y.L.; Huang, J.; Wu, Z.G.; Tao, W.Q. Numerical study of local heat transfer coefficient and fin efficiency of wavy fin-and-tube heat exchangers. *Int. J. Therm. Sci.* **2007**, *46*, 768–778.
22. Hatami, M.; Ganji, D.D.; Gorji-Bandpy, M. Numerical study of finned type heat exchangers for ICEs exhaust waste heat recovery. *Case Stud. Therm. Eng.* **2014**, *4*, 53–64.
23. Bai, S.Q.; Lu, H.L.; Wu, T.; Yin, X.L.; Shi, X.; Chen, L.D. Numerical and experimental analysis for exhaust heat exchangers in automobile thermoelectric generators. *Case Stud. Therm. Eng.* **2014**, *4*, 99–112.

24. Diesel fuel. Available online: [http://en.wikipedia.org/wiki/Diesel\\_fuel](http://en.wikipedia.org/wiki/Diesel_fuel) (accessed on 14 March 2015).
25. Lemmon, E.W.; Huber, M.L.; McLinden, M.O. *REFPROP Version 8.0, NIST Standard Reference Database 23*; US Department of Commerce: Washington, DC, USA, 2007.
26. Cengel, Y.A.; Boles, M.A. *Thermodynamics—An Engineering Approach*, 6th ed.; McGraw-Hill: New York, NY, USA, 2008; pp. 423–469.
27. Poling, B.E.; Prausnitz, J.M.; O’Connell, J.P. *The Properties of Gases and Liquids*, 5th ed.; McGraw-Hill: New York, NY, USA, 2001.
28. Roache, P.J.; Ghia, K.N.; White, F.M. Editorial policy statement on the control of numerical accuracy. *J. Fluids Eng.* **1986**, *108*, doi:10.1115/1.3242537.
29. Guo, Z.Y.; Li, D.Y.; Wang, B.X. A novel concept for convective heat transfer enhancement. *Int. J. Heat Mass Transf.* **1998**, *41*, 2221–2225.
30. Tao, W.Q.; Guo, Z.Y.; Wang, B.X. Field synergy principle for enhancing convective heat transfer—its extension and numerical verification. *Int. J. Heat Mass Transf.* **2002**, *45*, 3849–3856.
31. Guo, Z.Y.; Tao, W.Q.; Shah, R.K. The field synergy (coordination) principle and its applications in enhancing single phase convective heat transfer. *Int. J. Heat Mass Transf.* **2005**, *48*, 1797–1807.
32. Wang, E.H.; Zhang, H.G.; Fan, B.Y.; Ouyang, M.G.; Yang, K.; Yang, F.Y.; Li, X.J.; Wang, Z. 3D numerical analysis of exhaust flow inside a fin-and-tube evaporator used in engine waste heat recovery. *Energy* **2015**, *82*, 800–812.

© 2015 by the authors; licensee MDPI, Basel, Switzerland. This article is an open access article distributed under the terms and conditions of the Creative Commons Attribution license (<http://creativecommons.org/licenses/by/4.0/>).